REPORT DOCUMENTATION PAGE

Form Approved OMB NO. 0704-0188

The public reporting burden for this collection of information is estimated to average 1 hour per response, including the time for reviewing instructions, searching existing data sources, gathering and maintaining the data needed, and completing and reviewing the collection of information. Send comments regarding this burden estimate or any other aspect of this collection of information, including suggesstions for reducing this burden, to Washington Headquarters Services, Directorate for Information Operations and Reports, 1215 Jefferson Davis Highway, Suite 1204, Arlington VA, 22202-4302. Respondents should be aware that notwithstanding any other provision of law, no person shall be subject to any oenalty for failing to comply with a collection of information if it does not display a currently valid OMB control number.
PLEASE DO NOT RETURN YOUR FORM TO THE ABOVE ADDRESS.

1. REPORT DATE (DD-MM-YYYY)	2. REPORT TYPE	3. DATES COVERED (From - To)
	New Reprint	-

4. TITLE AND SUBTITLE	5a. CONTRACT NUMBER
High strength, nano-structured Mg–Al–Zn alloy	W911NF-10-1-0512
	5b. GRANT NUMBER
	5c. PROGRAM ELEMENT NUMBER
	611102

6. AUTHORS	
Baolong Zheng, Osman Ertorer, Ying Li, Yizhang Zhou, Suveen N. Mathaudhub, Chi Y.A. Tsao, Enrique J. Lavernia	5d. PROJECT NUMBER
	5e. TASK NUMBER
	5f. WORK UNIT NUMBER

7. PERFORMING ORGANIZATION NAMES AND ADDRESSES	8. PERFORMING ORGANIZATION REPORT NUMBER
University of California - Davis Sponsored Programs 118 Everson Hall Davis, CA 95616 -8671	

9. SPONSORING/MONITORING AGENCY NAME(S) AND ADDRESS(ES)	10. SPONSOR/MONITOR'S ACRONYM(S)
U.S. Army Research Office P.O. Box 12211 Research Triangle Park, NC 27709-2211	ARO
	11. SPONSOR/MONITOR'S REPORT NUMBER(S)
	58330-MS.1

12. DISTRIBUTION AVAILIBILITY STATEMENT

Approved for public release; distribution is unlimited.

13. SUPPLEMENTARY NOTES

The views, opinions and/or findings contained in this report are those of the author(s) and should not contrued as an official Department of the Army position, policy or decision, unless so designated by other documentation.

14. ABSTRACT

The mechanical behavior and microstructure of nanocrystalline (nc) Mg AZ80 alloy, synthesized via a cryomilling and spark plasma sintering (SPS) approach are reported and discussed. The effects of cryomilling processing on chemistry, particle morphology, and microstructure of the Mg alloy powder are described and discussed. The experimental results show that cryomilling for 8 h yields nc Mg agglomerates, approximately 30 μm in size, with an internal average grain size of approximately 40 nm. The

15. SUBJECT TERMS

Magnesium alloys, Nanocrystalline microstructure, Mechanical milling, Sintering

16. SECURITY CLASSIFICATION OF:			17. LIMITATION OF ABSTRACT	15. NUMBER OF PAGES	19a. NAME OF RESPONSIBLE PERSON
a. REPORT	b. ABSTRACT	c. THIS PAGE			Enrique Lavernia
UU	UU	UU	UU		19b. TELEPHONE NUMBER
					530-752-0554

Standard Form 298 (Rev 8/98)
Prescribed by ANSI Std. Z39.18

Report Title

High strength, nano-structured Mg–Al–Zn alloy

ABSTRACT

The mechanical behavior and microstructure of nanocrystalline (nc) Mg AZ80 alloy, synthesized via a cryomilling and spark plasma sintering (SPS) approach are reported and discussed. The effects of cryomilling processing on chemistry, particle morphology, and microstructure of the Mg alloy powder are described and discussed. The experimental results show that cryomilling for 8 h yields nc Mg agglomerates, approximately 30 ☐m in size, with an internal average grain size of approximately 40 nm. The mechanisms that are thought to be responsible for deformation twins that were observed in the cryomilled AZ80 powder are discussed. The cryomilled Mg powder was subsequently consolidated using SPS at 250, 300 and 350 ?C. The consolidated material consisted of a bimodal microstructure with nc fine and coarse grains formed in the SPS'ed Mg AZ80 microstructure. Inside of the coarse grains, nano-sized $Mg_{17}Al_{12}$ precipitates were observed. A maximum microhardness of 140 HV, compressive yield strength of 442.3 MPa, and ultimate strength of 546MPa are measured, which compare favorably to published values for conventional Mg alloys.

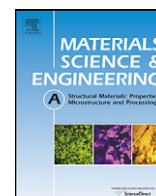# REPORT DOCUMENTATION PAGE (SF298)
(Continuation Sheet)

Continuation for Block 13

ARO Report Number   58330.1-MS
High strength, nano-structured Mg–Al–Zn alloy   ...

Materials Science and Engineering A

High strength, nano-structured Mg–Al–Zn alloy

Baolong Zheng[a], Osman Ertorer[a], Ying Li[a], Yizhang Zhou[a], Suveen N. Mathaudhu[b],
Chi Y.A. Tsao[c,d], Enrique J. Lavernia[a,*]

[a] Dept. Chem. Eng. Mater. Sci., University of California, Davis, One Shields Avenue, Davis, CA 95616, USA
[b] Weapons and Materials Research Directorate, U.S. Army Research Laboratory, Aberdeen Proving Ground, MD 21005, USA
[c] Dept. Mater. Sci. Eng., National Cheng Kung University, Tainan, Taiwan, ROC
[d] Frontier Materials and Micro/Nano Science and Technology Center, National Cheng Kung University, Tainan, Taiwan, ROC

ARTICLE INFO

ABSTRACT

The mechanical behavior and microstructure of nanocrystalline (nc) Mg AZ80 alloy, synthesized via a cryomilling and spark plasma sintering (SPS) approach are reported and discussed. The effects of cryomilling processing on chemistry, particle morphology, and microstructure of the Mg alloy powder are described and discussed. The experimental results show that cryomilling for 8 h yields nc Mg agglomerates, approximately 30 μm in size, with an internal average grain size of approximately 40 nm. The mechanisms that are thought to be responsible for deformation twins that were observed in the cryomilled AZ80 powder are discussed. The cryomilled Mg powder was subsequently consolidated using SPS at 250, 300 and 350 °C. The consolidated material consisted of a bimodal microstructure with nc fine and coarse grains formed in the SPS'ed Mg AZ80 microstructure. Inside of the coarse grains, nano-sized $Mg_{17}Al_{12}$ precipitates were observed. A maximum microhardness of 140 HV, compressive yield strength of 442.3 MPa, and ultimate strength of 546 MPa are measured, which compare favorably to published values for conventional Mg alloys.

© 2010 Elsevier B.V. All rights reserved.

1. Introduction

Mg alloys provide an opportunity to engineer light-weight structures, and interest in these materials has increased as one consequence of the global energy crisis. Mg alloys have advantages when used as structural materials, such as an attractive combination of low density of 1.74 g/cm^3 (35% lighter than Al, about 78% lighter than Fe) and high specific strength, along with good damping capacity, castability, weldability, machinability and recyclability [1–3]. Thus, Mg alloys have been widely used as replacement for Al alloys, as well as steel in weight-critical, automotive and aerospace structural applications. Mg alloys have also been used as an alternative to polymeric materials in the electronic and computer industries [1,4]. Despite some encouraging results, it is acknowledged that widespread application of Mg alloys has been hindered, in part, by their relatively low strength.

Strengthening of Mg alloys via the introduction of solid solution atoms and grain refinement additives represent effective approaches actively being researched and implemented. To that effect, much progress has been achieved in the development of high strength Mg alloys through solid solution strengthening using various types of solute atoms [5–7]. Review of the literature shows that

the highest tensile strength of cast Mg alloys reported thus far is 414 MPa, achieved in a Mg–18.2Gd–1.9Ag–0.34Zr (wt.%) alloy [8]. However, this Mg alloy system contains large amounts of rare-earth and noble metal elements for solid solution strengthening resulting in high costs for many practical applications.

Grain refinement via severe plastic deformation methods represents another recently proposed approach to achieve high strength in Mg alloys. It has been well established that nanocrystalline (nc) metals and alloys with grain sizes less than 100 nm generally exhibit significantly improved strength, an observation that has been partially attributed to the well known Hall–Petch mechanism [9,10]. Consequently, there are some studies describing the synthesis of nc Mg and its alloys using mechanical alloying at room temperature [11,12]. Other severe plastic deformation methods, such as equal channel angular pressing (ECAP) [13–15] and high pressure torsion (HPT) [16], have been reported to provide samples with no porosity and straightforward processing routes. However, these studies reveal that structural evolution of Mg during warm ECAP produces inhomogeneous grain/subgrain microstructures with sizes ranging around 1–20 μm and ultimate tensile strength (UTS) values of 329 MPa [15].

More recently, the cryogenic milling process has attracted considerable interest, primarily as a result of its ability to generate nc and non-equilibrium structures in relatively large quantities (i.e., up to 35 kg). Inspection of the scientific literature shows that this technique has been widely used to synthesize nc metals and alloys

* Corresponding author. Tel.: +1 5307524964.
E-mail address: lavernia@ucdavis.edu (E.J. Lavernia).

such as Al [10,17,18], Ni [19], Fe [20], and Ti [21]. The cryomilling technique possesses several characteristics that distinguish it from the conventional mechanical alloying process, including relatively high strain rates, large cumulative strains, and a cryogenic environment and temperature [10]. In related studies [10,18], it has been reported that the milling time required to reach the final grain size was significantly shorter in the case of cryomilling relative to that required of conventional milling performed at ambient temperature, which was attributed to the suppression of recovery mechanisms at cryogenic temperatures [22]. Moreover, review of the scientific literature reveals that published studies on the cryomilling of nc Mg alloys remain essentially non-existent, which provides a motivation for the present work.

The poor cold workability of the hexagonal close packed (HCP) crystal structure of Mg is largely responsible for its low formability at room temperature, and hence has limited the utilization of Mg as a wrought material. Among various commercial Mg alloys, the family comprising the Mg–Al–Zn ternary system (i.e., labeled as AZ alloys), is widely used for industrial applications. As an example, Mg AZ80 nominally contains 8.0 wt.% Al and 0.5 wt.% Zn with the addition of a small amount of Mn as an alloying element. It is a medium strength Mg alloy with good corrosion resistance and very good forging capability [23,24]. Therefore, the Mg AZ80 alloy system was selected and processed using a cryomilling and spark plasma sintering (SPS) synthesis route in this work. SPS is an attractive consolidation technique that was originally developed for sintering structural ceramics, metals and composite materials [25]. The SPS process is a pressure and pulsed current assisted sintering process utilizing on–off DC pulse energy. One of the advantages of the SPS

process is that it allows fabrication of bulk materials from powders using a fast heating rate and short thermal exposure cycle at low temperatures and thereby limits grain growth as compared to the commonly used hot pressing (HP) and hot isostatic pressing (HIP) approaches.

The present study seeks to provide insight into two important questions. First, what is it the influence of cryomilling on an hcp system, as represented by Mg? Second, is it possible to take advantage of a rapid sintering approach, as represented by SPS, to retain the nc structure in Mg and thereby attain increased strength? Accordingly, we synthesized nc Mg AZ80 alloy powders using the cryomilling technique followed by consolidation of these powders into bulk samples using SPS. Microstructural evaluation was performed using X-ray diffraction (XRD), scanning electron microscopy (SEM), and transmission electron microscopy (TEM). The microstructure and mechanical behavior of the SPS consolidated samples were then investigated using standard ASTM testing methods. The underlying deformation mechanisms are also discussed in an effort to elucidate fundamental phenomena in nc Mg alloys.

2. Experimental procedures

2.1. Cryomilling of MgAZ80 powder

The starting material used in this study was gas atomized Mg AZ80 powder with a chemical composition of 7.83 wt.% Al, 0.47 wt.% Zn, and 0.16 wt.% Mn. The starting powder, as shown in Fig. 1(a) and (b), exhibited an average particle size of 55 μm, distributed in the
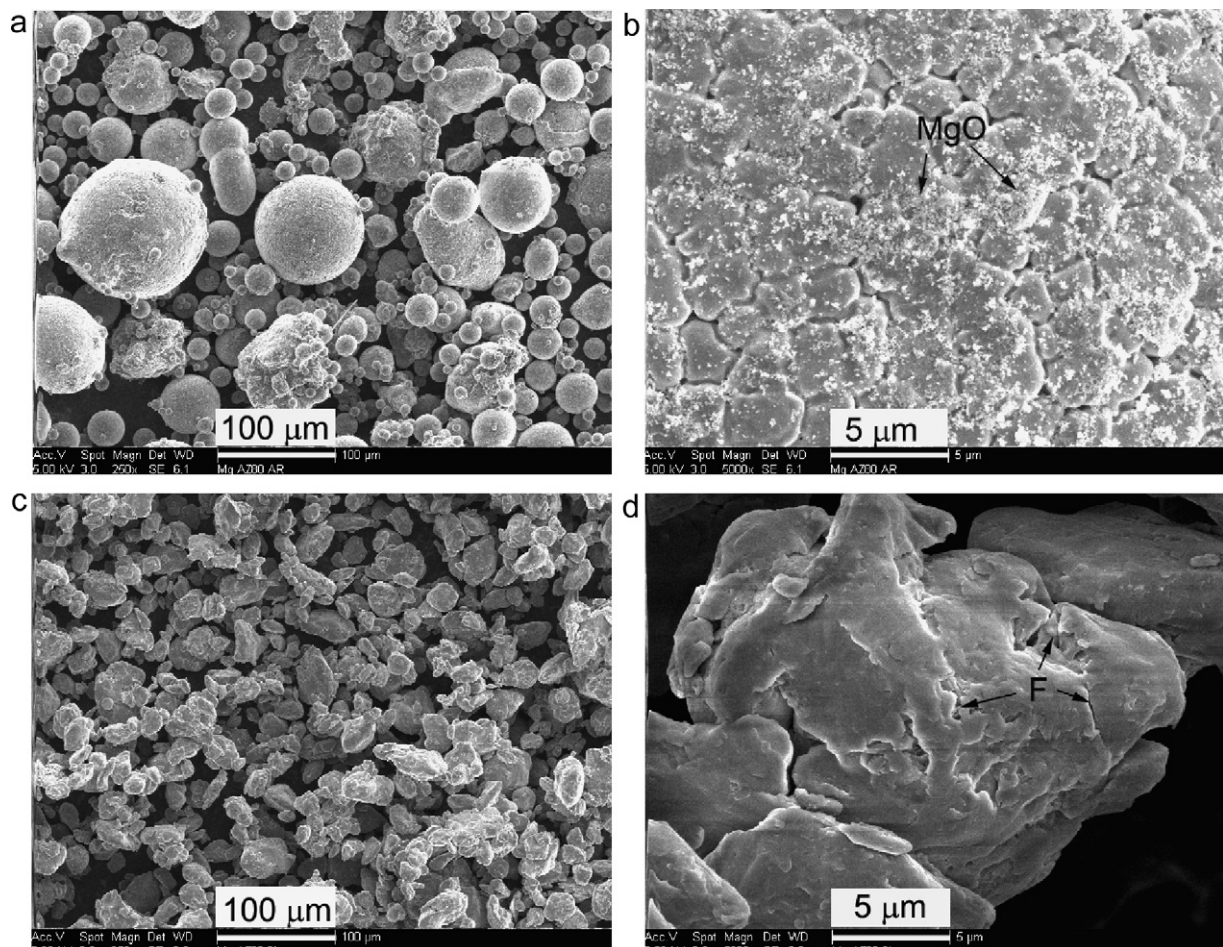

Fig. 1. SEM micrographs showing the morphology of (a and b) as-received gas atomized and (c and d) cryomilled Mg AZ80 powder.

Table 1
Cryomilling Mg powder using the large attritor with liquid Ar.

Experimental conditions	
Mill	Szegvari Attritor, 1-S, Union Process Co.
Container (tank)	Stainless steel
Atmosphere	Liquid argon
Milling temperature	−185.9 °C, 1 atm
rpm	180
BPR	60:1
Balls	6.4 mm diameter, stainless steel (20 kg)
Powder	Mg AZ80 (350 g)
Milling time	8 h

range 10–106 μm with a spherical morphology. Oxide phases, with discontinuous and non-uniform distribution, were observed on the Mg AZ80 powder surfaces, as commonly reported for atomized metal powders.

The cryogenic milling experiment was performed with liquid Ar at temperatures −186 °C. A modified 1-S Szegvari-type Attritor (Union Process, Inc., Akron, OH) was used in a stainless steel tank and an impeller with stainless steel balls (with diameter of 6.4 mm). Liquid Ar was continuously introduced into the tank during the milling by a temperature controller with an attached thermocouple to maintain a constant liquid level in the tank. The Mg powders were cryomilled for 8 h with a ball-to-powder ratio (BPR) of 60:1 (w/w) and an impeller rotation speed of 180 rpm. The experimental parameters are shown in Table 1. In order prevent atmospheric contamination and to mitigate the hazards associated with the reactivity of Mg, the powders were always handled in an inert atmosphere using a closed transfer container and an Ar glove box.

2.2. SPS of nc MgAZ80

Bulk nc Mg AZ80 alloy samples were fabricated via SPS from the cryomilled powders. Powders obtained after cryomilling were consolidated by an SPS-825S DR.SINTER apparatus (SPS Syntex Inc., Japan) with maximum pulse DC output 12 V and 8000 A under a vacuum condition (lower than 6 Pa). Prior to SPS processing the cryomilled powders were loaded in a graphite die (20 mm diameter) in an Ar glove box to minimize oxidation of Mg powder. SPS was performed at different temperatures with 3 min of holding time while a heating rate of 120 °C/min, a sintering pressure of 100 MPa were used, as listed in Table 2. The purpose of using different sintering temperatures was to investigate its influence on density and mechanical behavior.

The cross-sectional microstructure of cryomilled powders and fracture surfaces of the SPS fabricated bulk nc Mg AZ80 samples were observed using a SEM operated at 5 kV. Thin foils for TEM observations were prepared via mechanical grinding and polishing to a thickness of about 30 μm, followed by ion milling to a thickness of electron transparency was carried out using a Gatan precision ion polishing system (PIPS) 691 with an Ar accelerating voltage of 4 kV from both sides until perforation occurred. XRD with CuK-α radiation was utilized for phase identification and grain size calculations. The compression behavior of the consolidated bulk materials at ambient temperatures was measured using an Instron 8801 universal testing machine (Norwood, MA) equipped with a video extensometer. Cubic compression spec-

Table 2
Process conditions for SPS sintering cryomilled Mg AZ80 powder.

Sample	Powder	Temperature (°C)	Pressure (MPa)	Time (min)
0	Gas atomized	350		
1		350		
2	Cryomilled	300	100	3
3		250		

imens (4 mm × 4 mm × 4 mm) were electrodischarge-machined (EDM). Prior to testing, the surfaces of all test specimens were polished to remove any oxide layers present. Compression studies were performed at a crosshead velocity of 0.001 mm/s until failure.

3. Results and analysis

3.1. Cryomilled AZ80 powder

3.1.1. Particle size and morphology

Fig. 1(c) and (d) shows the typical particle morphologies of Mg Az80 powder as they evolved after 8 h cryomilling. The final particle size distribution was homogenous and ranged between 10 μm and 40 μm with an irregular, but close to spherical morphology. During the early stages of cryomilling, the morphology of a large proportion of powder particles is modified from spherical to disc-like due to the severe plastic deformation induced by ball–powder–ball collisions and shearing as reported in related studies [10,26,27]; this is followed by a period of cold welding and fracturing of Mg particles. As the particles work harden, they fracture more readily; hence the average particle size tends to decrease and as the spherical morphology is recovered with increasing milling time. This observation is consistent with the mechanism Benjamin and Volin proposed to explain particle size evolution during mechanical milling [28]. Fig. 2 shows the cross section of the cryomilled Mg powders, indicating a cryomilling mechanism of cold welding (w) and fracturing (f). Cryomilling up to 8 h corresponds to the stage where the welding and fracturing processes are competitive and continuous. The decrease in the average particle sizes indicates a stage of fracture dominance. This suggestion is consistent with the presence of a liquid Ar environment, which at a temperature of −186 °C is likely to hinder recovery processes, and thereby facilitate rapid hardening and fracture. The cold welding and fracturing processes are strongly dependent on the powder characteristics and milling conditions [10,28].

The effect of milling time on the average particle size provides an indication of the rates at which cold welding and fracturing occur during cryomilling. The time variation of the total number N of particles in the Mg system can be written as [29]:

$$\frac{N}{N_o} = \exp\frac{(\alpha_f - \alpha_w)t}{\tau_p} \tag{1}$$

where the terms α_f and α_w represent the probability of a fracture or welding event occurring in a specific impact, changing as a function of milling time and particle morphology, and τ_p is the time between impacts for an average particle, and N_o is the initial total number of particles. In the case of HCP Mg only two independent slip systems are active at ambient temperature and hence even fewer slip systems will be active at the liquid Ar temperature of −186 °C [3,30], hence their inherently low ductility. Therefore, the probability of a fracture, α_f, of HCP Mg alloys is higher than that corresponding to BCC and FCC alloys, leading to a rapid increase in the particle number N. This leads to a rate of decrease in particle size which is higher than that corresponding to widely studied Al systems. The average particle size of Mg AZ80 powder after cryomilling in liquid Ar for 8 h is 17.8 μm, but the average particle size of cryomilled pure Cu powder, for example, is 34.2 μm, and the average particle size of cryomilled Al 5083 powder is 91.2 μm [27].

3.1.2. Chemical analysis

Chemical analysis of the as-received and the milled powders was carried out by a commercial laboratory (Luvak Inc., Boylston, MA). The chemical analysis results for oxygen, nitrogen, iron, magnesium, aluminum, zinc, and manganese contents are summarized in Table 3. The amount of Ar was not measured given the difficulties associated with Ar analysis. The results reveal an increase in
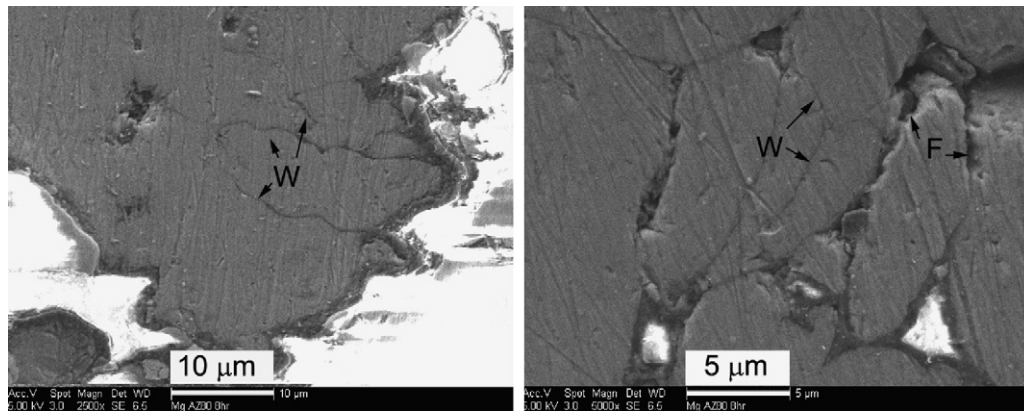
Fig. 2. The cross section of the cryomilled Mg powders, indicating a cryomilling mechanism of cold welding and fracturing.

the amount of nitrogen and iron during cryomilling, but a slight decrease in the amount of oxygen. Powder contamination is an inherent characteristic of mechanical milling, and this may arise from either of the processing media and/or the atmosphere. The Fe contamination stems from the wear of the stainless steel milling balls, tank, and shaft during cryomilling. The nitrogen is introduced into the powder during powder exposure to air, because of the high surface area of cryomilled Mg powder and its high tendency to react with nitrogen [10]. The surface area prior to and following cryomilling has been measured and the results show a 10-fold increase in surface area, A, and surface to volume ratio, A/V, after cryomilling [31]. The increased surface area, in combination with the chemical activity of Mg facilitates surface adsorption of gaseous atoms. The slight decrease in oxygen analysis is not considered to be statistically relevant, given the difficulties associated with chemical analysis for this element. The oxygen in the cryomilled powder is present as brittle oxide particles, which are uniformly dispersed throughout the microstructure [32]. For other added elements (i.e., Al and Zn) alloying occurs and chemical homogeneity was achieved after 8 h cryomilling, as discussed in the phase analysis that follows.

3.1.3. Grain size and phase identification

XRD profiles for as-received gas atomized Mg AZ80 powder and cryomilled Mg AZ80 powders are shown in Fig. 3. Significant peak broadening from strong peaks was observed for cryomilled Mg AZ80 powder, as compared to those of the gas atomized powder. This peak broadening is attributed to the reduced crystallite size and the high internal residual microstrain introduced during cryomilling.

The initially sharp diffraction peaks of the Mg phase significantly broadened after cryomilling. The strain broadening may be closely approximated by a Gaussian function, whereas the effects of small crystalline size distributions more closely resemble a Cauchy broadening profile. When both the effects are responsible for peak broadening the combined relation may be expressed by the following equation [33]:

$$\frac{B^2}{\tan^2 \theta_o} = \frac{K\lambda}{D} \left[\frac{B}{\tan \theta_o \sin \theta_o} \right] + 16e^2 \tag{2}$$

where θ_o is the position of peak maximum, and K is a factor, being taken as 0.94, λ is the wavelength of the X-ray radiation, θ_o is the Bragg angle of a peak in radians, D is the average grain size, e is the microstrain, and B is the integral width. By performing a least squares fit to $B^2/\tan^2 \theta_o$ against $B/(\tan \theta_o \sin \theta_o)$ for all of the measured peaks of a sample. From the slope, $K\lambda/D$, the average grain size is calculated to be 39.5 nm for Mg AZ80 powders after 8 h cryomilling.

As shown in the XRD patterns in Fig. 3, Mg peaks are evident after cryomilling, indicating that the milled Mg powders primarily consist of a single Mg phase. Most of the alloying elements of Al and Zn atoms in the cryomilled Mg are thought to be in solid solution, while some small peaks corresponding to Mg oxide MgO were found possible due to the reaction with oxygen when cryomilled Mg powder was exposed to air during XRD testing. Cast AZ80 alloy usually contains a large fraction of $Mg_{17}Al_{12}$ precipitates along the grain boundaries. The small peaks corresponding to the intermetallic compound of $Mg_{17}Al_{12}$ were also shown in the XRD curve of starting gas atomized Mg AZ80 powder. These peaks are least evident and almost disappeared in the 8-h cryomilled Mg powder XRD curve. The formation of fine oxide particles may considered as results from the gas atomized powder and the interaction between Mg and O from the surrounding environment.
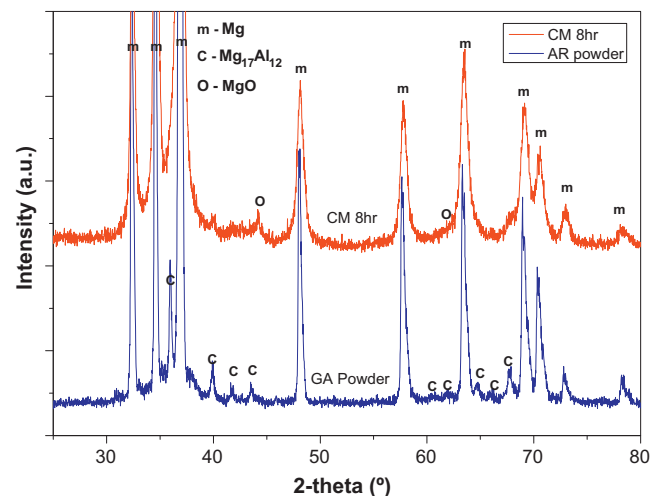
Table 3
The chemical analysis results of the gas atomized and cryomilled Mg AZ80 powders (wt.%).

Elements	Gas atomized	Cryomilled
Magnesium	90.8	89.5
Aluminum	7.83	7.6
Zinc	0.47	0.46
Oxygen	0.074	0.065
Nitrogen	0.029	1.18
Manganese	0.16	0.15
Iron	0.023	0.058

Fig. 3. The XRD pattern of as-received gas atomized and cryomilled Mg AZ80 powders.
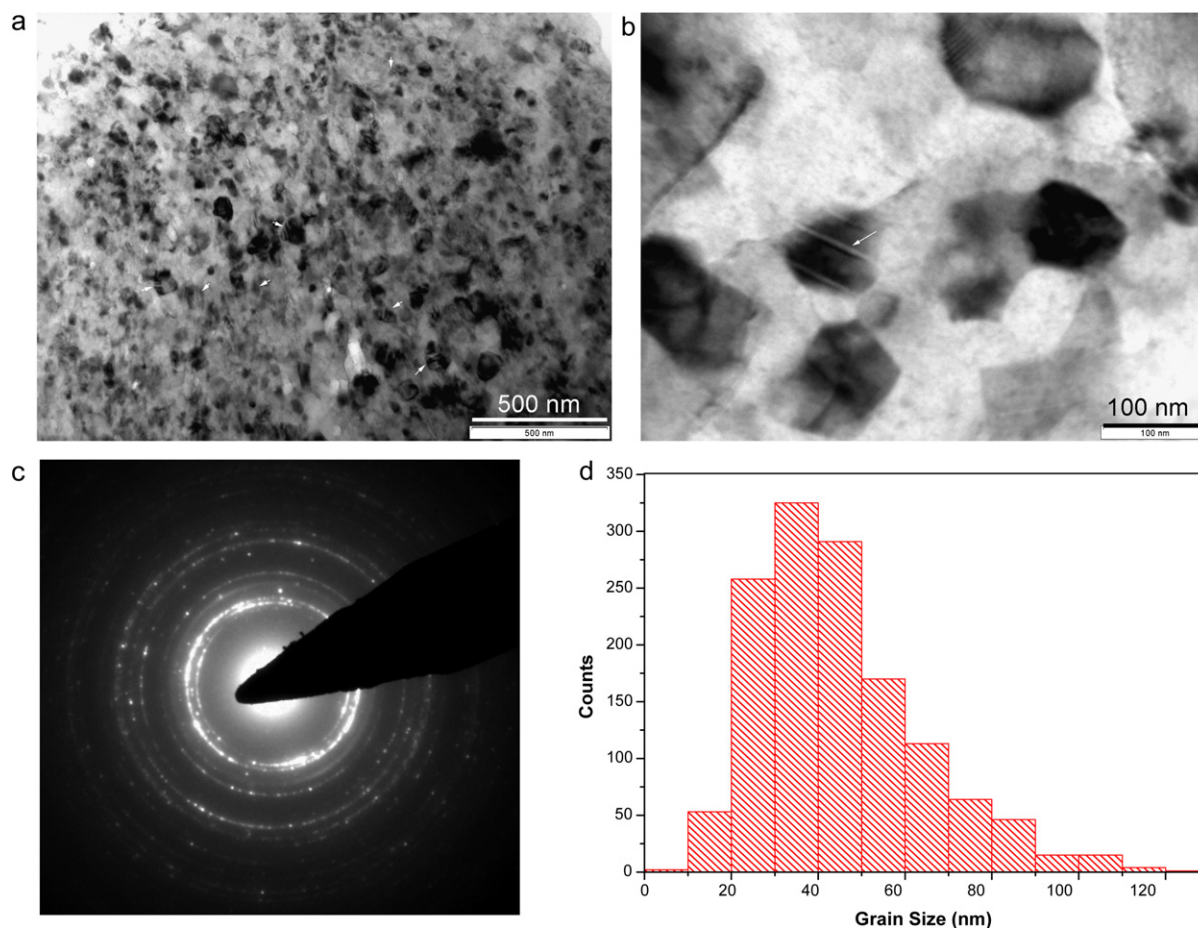
Fig. 4. TEM micrograph of cryomilled Mg AZ80 powders: (a and b) bright-filed image of Mg powder after 8 h milling, (c) its correspondent SAED, and (d) histograms of grain size distribution of cryomilled nc Mg AZ80 powders.

The microstructure of the as-cryomilled powders was also investigated in detail using transmission electron microscopy (TEM). Fig. 4 shows the TEM micrographs and selected area electron diffraction (SAED) pattern of the nano-structured Mg powder after cryomilling. Equiaxed grains distributed in the size range from 10 to 120 nm and separated with well defined grain boundaries were observed. The average grain size calculated is to be 41 nm based on more than 300 measured grains. This result is consistent with the grain size measured from the broadening of XRD patterns. As shown in Fig. 4(c), the SAED pattern of the Mg grains shows a ring pattern, indicating that the individual grains are nc in size and separated by high-angle grain boundaries with a random orientation. It is interesting to note that some deformation twins were observed as indicated by the arrow in Fig. 4(b), similar to the deformation twins observed in the nc Mg–Ti alloy [34]. Within twin domains the lattice is sheared and reoriented and it is several nanometers to sub-micrometers in thickness. Deformation twins are easily formed in deformed coarse grained Mg alloys due to the low stacking fault energy (SFE) of pure Mg (measured 78 mJ/m^2 [35] and calculated around 30 mJ/m^2 [36]) in combination with a limited number of independent slip systems. Moreover, alloying Mg with Al and Zn, as in Mg AZ80, also effectively decreases the SFE, thereby facilitating twinning as it could be a result of decreasing SFE [37]. The SFE in Mg–(3–9 wt.%) Al alloys is 5.8–27.8 mJ/m^2, and decreases with increasing Al content [38]. The presence of high local stresses during cryomilling, in combination with limited availability of slip systems and a decreased SFE are all factors that will contribute to the activation of the main pyramidal slip system in Mg, and twinning will take place by plane displacement and atomic shifting [39].

Fig. 4(d) shows the overall grain size distribution for cryomilled Mg AZ80 powders. A majority of the grains were distributed in the size range of 20–60 nm, while some coarse grains were documented as large as 120 nm.

3.2. Spark plasma sintered MgAZ80

3.2.1. Microstructure characterization

The SPS process represents a multiple-field problem in which the electric, thermal and displacement (i.e., shrinkage) fields are intimately coupled via a material response. This problem is strongly nonlinear since each field interacts with each other and affects the properties of SPS'ed materials. In SPS the as-sintered density is dominated by both the packing density as well as the rate of shrinkage. Fig. 5 shows the variation of displacement of a graphite die punch units as a function of heating temperature for different sintering temperature and powders. The 1st shrinking regime occurred with increasing temperature while the applied pressure of 80 MPa remained constant. The 2nd shrinking regime occurred with increasing pressure up to 100 MPa while the heating temperature was kept constant. The cryomilled Mg AZ80 powder began shrinking at about 65 °C, whereas the gas atomized powder began to shrink at 115 °C due to their different physical response (i.e., thermal stability), geometry (i.e., different surface area and morphology) and distribution of phases present (i.e., nitrides and oxides). The observed shrinkage is related to the complex deformation behavior of each particle, which also depends on internal defects (i.e., grain boundaries, dislocations, twins, vacancies, etc.), as well as the local pressure and temperature at the interface
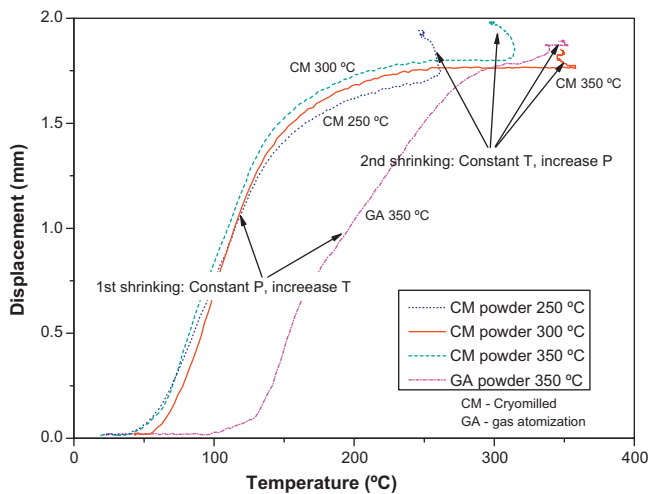
Fig. 5. Displacement variation of die punch as a function of heating temperature.

between particles. The lower shrinkage threshold observed for the cryomilled powder is thought to be related to the increased density of interfaces that are introduced during deformation which may readily accommodate and dissipate strains during loading. In addition to a higher packing density and surface energy, cryomilled powders inherently have a high fraction of contact interfaces that are likely to promote higher local current density and electrical resistance during SPS processing. Therefore, the smaller cryomilled particles will undergo faster deformation and densification relative to the gas atomized particles.

XRD studies were carried out to identify existing phases as well as variations in grain size in the SPS'ed samples. Fig. 6 shows a comparison between the XRD profiles of the SPS'ed bulk samples and the cryomilled Mg powders. The experimental results show that the grain size of Mg AZ80 increases during SPS process as the XRD peaks of SPS'ed samples are narrower when compared to those of the as-cryomilled powder. The specific variation of grain size was also observed with TEM. The results show the presence of the intermetallic compound, body-centered cubic $Mg_{17}Al_{12}$ in all of the SPS'ed bulk samples, indicating that $Mg_{17}Al_{12}$ precipitation and growth occurred during SPS processing presumably due to thermal and strain activation [40].

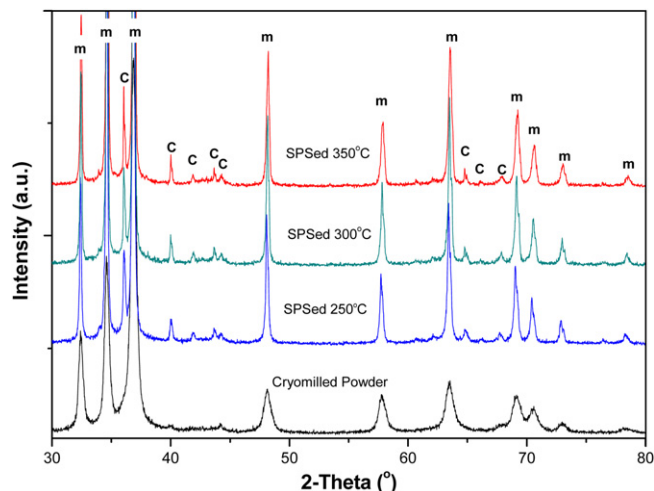Fig. 7 shows the typical TEM micrographs and corresponding selected area electron diffraction (SAED) pattern for SPS'ed Mg samples. Grain sizes distributed in the size range of 200 nm to 1 μm were observed at the interface area between the nano-grained powder particles, effectively leading to a bimodal nanostructure in the Mg AZ80 materials. To that effect, in the case of the sample SPS'ed at 350 °C, the mean grain size of the fine grain (FG) matrix is measured to be approximately 68.9 nm, which is slightly larger than that of the as-cryomilled Mg powder, presumably suggesting limited grain growth. In comparison, the mean grain size of the coarse grained (CG) region (total 5% in vol.) at the interfaces of particles is measured to be 495.3 nm. The corresponding histograms for the grain size distributions of SPS'ed Mg AZ80 materials are shown in Fig. 8. The grains at the particle interfaces appear to have experienced more coarsening when compared to those inside of the particles, leading to the observed bimodal nanostructure. The presence of nano-pores, approximately 100–200 nm in size was also documented as shown with arrows (P) in the TEM micrograph of Figs 7(a) and (c), and 9(a), although the measured density can reach 1.83 g/cm³, which is higher than that of theoretical density of AZ80 (1.81 g/cm³) presumably attributable to the presence of oxide particles or other element contamination in the SPS'ed samples. The density increases with SPS sintering temperature increasing from 250 °C to 350 °C. The density was measured with the method of hydrostatic weighing in an ethyl alcohol solution. The origin of the nano-pores found in the SPS'ed Mg AZ80 materials is not completely understood at present. One possible source for the observed pores is thought to be the physical entrapment of Ar in the cryomilled Mg AZ80 powder. Even though there is none or very limited chemical adsorption or solubility of Ar in Mg alloys [3], it is possible for Ar to have been physically adsorbed on the surface of Mg alloys during cryomilling in liquid Ar environment. The continuous folding, cold working and fracture of metallic surfaces during milling in a liquid Ar environment all facilitate internal gas entrapment. As such, increased milling times will lead to additional exposure of clean metal surfaces/interfaces to the Ar environment resulting to increases in Ar concentration in the milled powder. The combination of an essentially zero solubility of Ar in the Mg lattice, with thermal activation of the Ar atoms during SPS processing are likely to promote coalescence of the Ar atoms and the eventual nucleation of pores. Therefore, degassing of cryomilled Mg AZ80 powder is necessary to remove any entrapped Ar prior to consolidation of the cryomilled powder. The vacuum level that is present during SPS is limited to the 2–6 Pa range, and hence it is unlikely to promote complete degassing of the Ar during sintering. Hence, any gas present at the interfaces of the cryomilled powder is likely to form isolated voids during densification.

Inside of the coarse grains, nano-sized $Mg_{17}Al_{12}$ precipitates (30–90 nm) were observed. These are illustrated with arrows in Fig. 9(a). Energy Dispersive X-ray Spectroscopy (EDX) quantitative analysis, in combination with TEM, was used to measure the relative amounts elements in precipitated particles. The results, as shown in Fig. 9(b), indicate that the precipitated particles contain more Al than that of matrix, which implies that the precipitated particles are possibly $Mg_{17}Al_{12}$ intermetallic phase, based on phase diagram considerations and published results [24,41,42]. The relative concentrations of Mn and Zn are also higher around the precipitated particles than that in the matrix.

The phenomena responsible for the formation of the observed bimodal nanostructure in the SPS'ed Mg AZ80 can be rationalized on the basis of the conditions associated with the SPS process, which involves an electrical spark discharge phenomenon. In particular, spatial variations in the thermal and stress fields are likely to conditions that can locally promote grain growth. During SPS, a pulsed current passes though both die and conductive powder, which will promote thermal energy and mass transfer. The thermal energy generated in the graphite die from Joule heating, is transferred to the powder via radiation and conduction; however, local
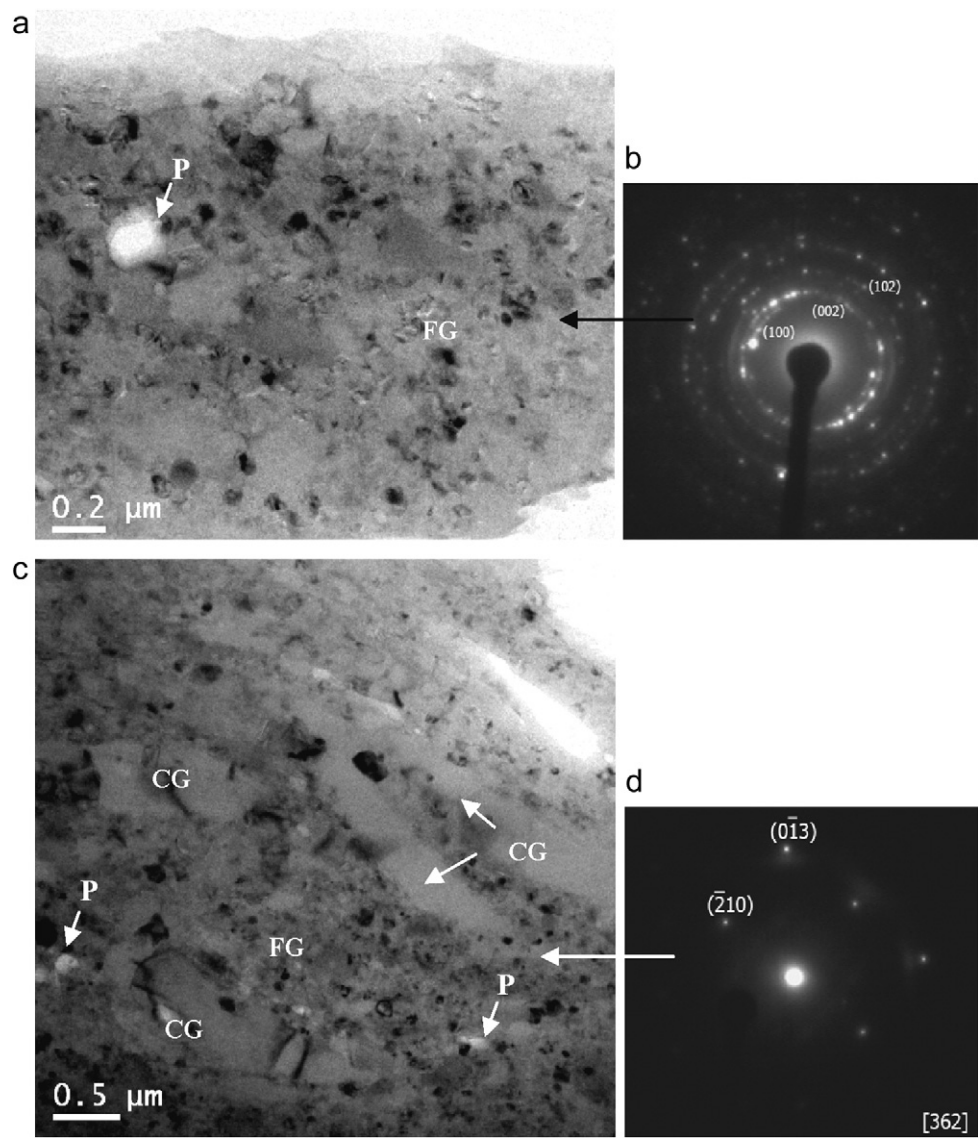

Fig. 6. XRD patterns of SPS'ed cryomilled Mg AZ80 powder.

Fig. 7. TEM micrograph of SPS'ed Mg AZ80 bulks: bright-filed image, and its correspondent SAD of (a and b) fine and (c and d) coarse grain.
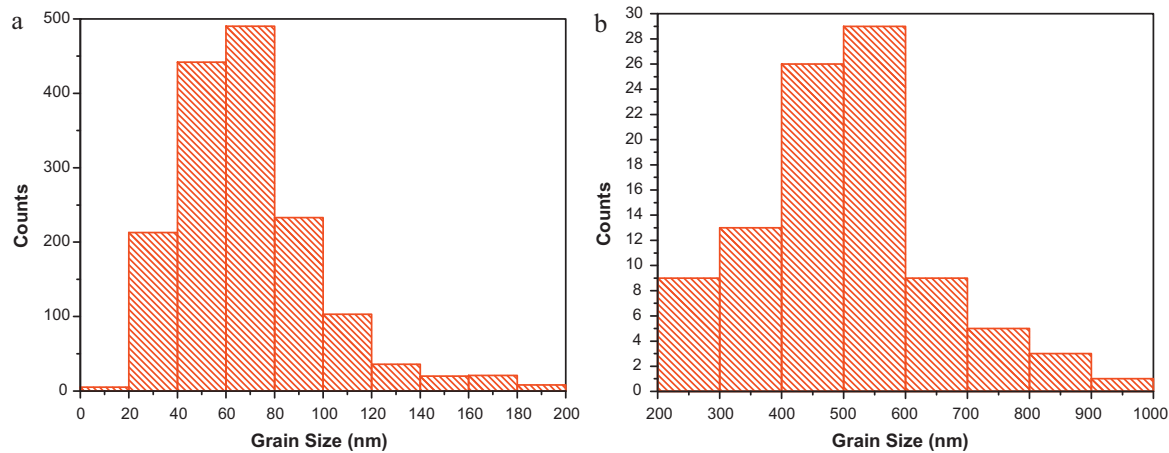

Fig. 8. Histogram of grain size distribution of SPS'ed Mg AZ80 in (a) fine and (b) coarse grain area.
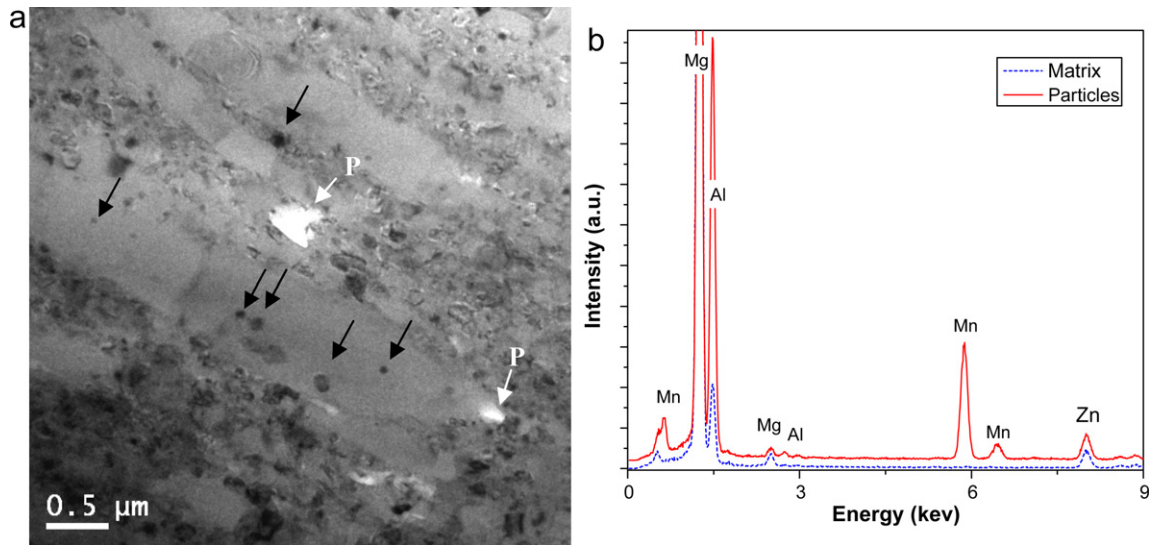
Fig. 9. TEM micrograph of SPS'ed Mg AZ80 bulks showing precipitated particles in coarse grains.

increases in temperature will occur from the combination of a small contact area and a high local current density. The heat transfer in sintered particles can be expressed in the thermal energy equation as follows [43]:

$$\frac{1}{r^2}\frac{\partial}{\partial r}\left(kr^2\frac{\partial T}{\partial r}\right) + \frac{1}{r^2\sin^2\theta}\frac{\partial}{\partial\phi}\left(k\frac{\partial T}{\partial\phi}\right)$$
$$+ \frac{1}{r^2\sin\theta}\frac{\partial}{\partial\theta}\left(k\sin\theta\frac{\partial T}{\partial\theta}\right) + \dot{q} = \rho c_p\frac{\partial T}{\partial t} \qquad (3)$$

where ρ is density, c_p is specific heat, and q is energy rate generated per unit volume for conduction analysis with spherical coordinates (r, Φ, θ). In the case of micron-sized metallic particles, the internal temperature is equilibrated within several milliseconds. However, during SPS processing, the continuity of the electric field is disrupted by the presence of multiple interfaces. A local increase in temperature from electrical Joule heating can be calculated using Joule's law, as:

$$T = \frac{I^2Rt}{mc_p} \qquad (4)$$

where I is the electric current, R is electric resistance, t is time, m is the mass, and c_p is the specific heat of SPS'ed material. It has also been proposed that a spark discharge may occur at inter-particle regions [25], leading to localized partial melting and perhaps even to the formation of a metallic vapor (or plasma, whose existence has yet to be unambiguously demonstrated [44]) as a result of elevated localized temperatures. Under the influence of the pressure, thermal and electromagnetic fields, constricted geometries or "necks" are formed around the contact area between the particles. These necks gradually develop and plastic deformation progresses during sintering, resulting in densification. Meanwhile, significant grain growth is possible in the contact area between particles due to the activation of localized higher temperature and stress [45,46]. Fig. 10(a) illustrates the phenomenon of neck formation during spark plasma sintering. Plastic deformation and thermal field diffusion simultaneously promote mass transport, as shown in Fig. 10(b), which illustrates mass transfer path during SPS sintering. In addition to conventional particle volume diffusion, surface diffusion, grain boundary diffusion, and plastic flow, SPS processing may also promote partial melting and consequently, welding due to local electric discharge effects [25]. The energy associated with the discharge and mass transport through the powder is propor-
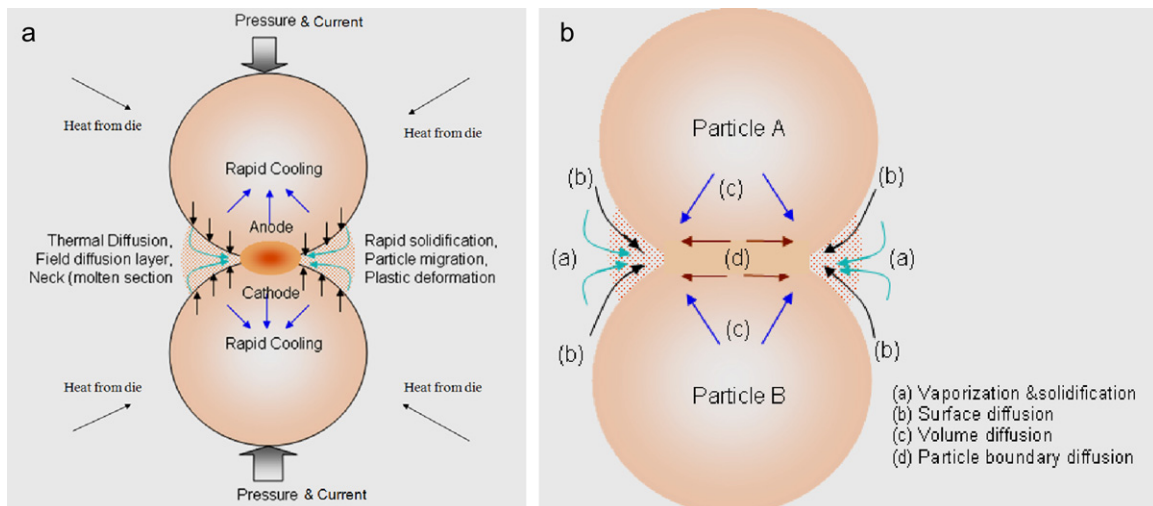

Fig. 10. Illustration of (a) heat transfer between particles and (b) mass transfer paths during SPS processing.
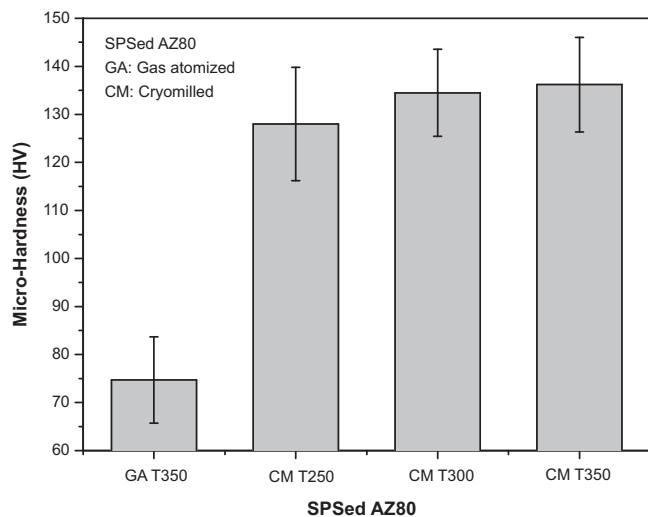
Fig. 11. Variation of microhardness measured with different processed conditions.

Fig. 12. Compressive properties of SPS'ed Mg AZ80 with cryomilled powder.

tional to the current flow. The role of the current depends on the process and the nature of processed materials. On the basis of the electro-migration theory, the effects of current (Joule heating) on mass transport can be evaluated with the flux of diffusing species, J_i [47]:

$$J_i = -\frac{D_i C_c}{RT}\left[\frac{RT\partial\ln C_i}{\partial x} + Fz^*E\right] \tag{5}$$

where D_i and C_i are the diffusivity and concentration of ith species, respectively. E is the field, R is the gas constant, T is the temperature, F is Faraday's constant, and z^* is the effective charge in the species. The mass transport increases with increasing electromagnetic field and effective charge. In related work, Munir et al. demonstrated that the imposition of current has a pronounced effect on mass transfer during SPS processing [44].

The above discussion suggests that whereas the local thermal and stress fields that are present at or in the vicinity of interfaces are likely to promote grain growth, the microstructure in the interior of the powders is likely to remain unaffected. It is based on these arguments that the observed presence of a distribution of bi-modal grain sizes can be rationalized.

3.2.2. Mechanical behavior

Room temperature compression and microhardness studies were utilized to provide insight into the mechanical behavior of cryomilled, SPS'ed MgAZ80 samples. Fig. 11 shows the variation of microhardness for SPS'ed samples processed at different temperatures. The microhardness of the cryomilled and SPS'ed samples is twice as high as that of the gas atomized and SPS'ed material, and moreover it increases with increasing SPS sintering temperature and a concomitant increase in density. The maximum measured microhardness was 146 HV, with a corresponding tensile strength (∼1/3 hardness) estimated to be 515 MPa,
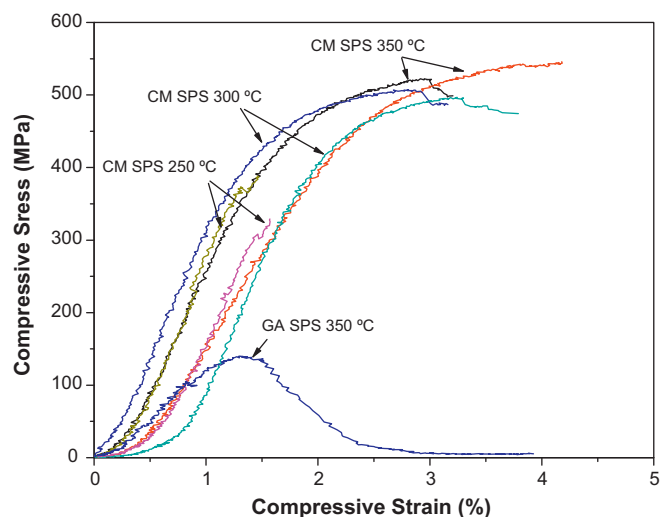
which is significantly higher than the values for conventional Mg alloys.

Fig. 12 shows the compression behavior of materials with different process parameters. Relevant mechanical properties are summarized in Table 4. The measured highest ultimate strength value for cryomilled and SPS'ed MgAZ80 is 545.9 MPa with 4.2% strain at failure. This is the highest strength of Mg alloys reported thus far, and compares favorably with the reported high strength of 329 MPa for rolled Mg AZ80 sheets [41]. In related studies on mechanical alloyed Mg–5%Al alloy followed by sintering and extrusion, a strength value of 500 MPa with a ductility value of 3% was reported [48]. The reported highest strength or as-cast Mg is less than 414 MPa with an elongation of less than 2% [8], achieved in the Mg–18.2Gd–1.9Ag–0.34Zr (wt.%) system. The highest measured yield strength of SPS'ed nanostructured Mg AZ80 samples is 442.3 MPa, which is considerable higher than that of conventional wrought Mg AZ80 alloys (∼200 MPa) [24]. The strength values measured for SPS samples increase with increasing sintering temperature. Despite the fact that temperature increase facilitates grain growth, clearly the extent of densification in this temperature range plays a more important role in strengthening.

4. Discussion

4.1. Deformation behavior

During cryomilling of Mg AZ80 alloy powder, severe cold deformation leads to particle flattening, welding and fracturing. However, at the micro-scale, the formation of nano-sized grains is more complex, which involves three stages for grain refinement [49]: (1) localized deformation in shear bands leads to high density of dislocations; (2) these dislocations annihilate and rearrange to form small-angle grain boundaries, which separate the indi-

Table 4
Summary of compressive properties of SPS'ed cryomilled Mg AZ80.

No.	Samples	Sample no.	Yield strength (MPa)	Ultimate strength (MPa)	Strain at failure (%)
1	CM SPS 350 °C	1	442.3	545.9	4.2
		2	414.5	552.3	3.2
2	CM SPS 300 °C	1	423.4	507.4	3.8
		2	421.8	496.8	3.2
3	CM SPS 250 °C	1	386.8	388.2	1.5
		2	327.3	329.0	1.6
4	GA SPS 350 °C	1	125.1	140.1	–

CM: cryomilling; GA: gas atomization; SPS: spark plasma sintering.

vidual crystallites, exhibiting nano-sized sub-gains after certain strain level of deformation; (3) the transformation of the sub-gains boundary structure to randomly oriented high angle grain boundaries. The deformation enters a steady state, when the dislocation generation rate is balanced by the annihilation rate. In the case of cryomilling, energy is stored in the form of lattice defects, such as dislocations and vacancies. The low temperature renders recovery more difficult by limiting the mobility of dislocations [22].

Plastic deformation of Mg AZ80 alloy powder during cryomilling occurs via the glide of dislocations as well as via twinning. Generally, Mg alloys show only limited formability and ductility at ambient temperature. As previously discussed, 5 independent slip systems must be active for polycrystals to deform uniformly without failure at the grain boundaries [50]. The two most common slip systems in HCP Mg alloy are basal $(0\,0\,0\,1)\,\langle 1\,1\,-2\,0\rangle$ and prismatic $(1\,-1\,0\,0)\,\langle 1\,1\,-2\,0\rangle$ slips, which offer only four independent modes between them, and is not sufficient to satisfy the von Misses criterion [50]. Thus, to improve plasticity of Mg alloys, non-basal slip systems should be activated.

The low temperature brittleness of Mg results from the restricted number of independent operative slip systems. Therefore, the low temperature deformation behavior of Mg AZ80 alloys in liquid Ar during cryomilling is governed by the activity of non-basal slip systems and by twinning. The activity of a slip system depends on the critical resolved shear stress (CRSS). The high stress value that is required to activate a non-basal slip system may facilitate deformation via twinning. The CRSS for the non basal slip systems of Mg alloys strictly depends very significantly on temperature, and decreases with increasing temperature. At room temperature, the CRSS for prismatic slip is about 100 times higher than that of basal slip, whereas it is only 4 times higher at 300 °C [51]. Their ductility could obviously improved between 200 °C and 225 °C depending on the Mg alloy composition [52], while the pyramidal planes could lead to an erratic increase in the plastic deformation activated above 225 °C. However, because the temperature of cryomilling AZ80 with liquid Ar is about −186 °C, even a local deformation temperature increase will be limited thereby hindering activation of the pyramidal slip system; one possible mechanism that can be activated under these conditions is deformation twinning.

Twinning, as a deformation mechanism, can be activated under conditions of elevated stress concentration, low temperatures and high strains. Therefore, deformation twinning in AZ80 is likely to be activated during cryomilling as shown in Fig. 4(b). Twinning plays a role as important as slip in the plastic deformation of HCP Mg alloys. Twin growth/thickening triggered with the decomposition of slip dislocations at a twin interface into twinning dislocations [53]. One effect of twinning on the plastic deformation is that unfavorably oriented grains for slip and twinning are reoriented into a more favorable orientation during twinning. Therefore, the total plastic strain of nc Mg alloys can be increased in the presence of twinning, as results found in nanotwined Cu [54]. The formation of deformation twins is also prevented by grain refinement due to the activation of non-basal slip systems [55] and grain boundary sliding [56]. Hence, the ductility of nc Mg AZ80 is negatively influenced by the lack of extensive dislocation activity in the nc grains, limited slip systems in the HCP structure, and of the presence of nano-pores in the SPS'ed Mg alloy. These results suggest that controlling texture and promoting nanotwin formation represent excellent strategies to engineer ductility in nc Mg alloys. Studies are underway to test the validity of this hypothesis.

4.2. Bimodal microstructure

Bulk nc metals and alloys generally exhibit high strength but this is also accompanied by limited ductility at room temperature dur-

ing plastic deformation, a behavior that is attributable to the lack of extensive dislocation activity during deformation [57]. The low ductility of nc materials is detrimental to their overall toughness behavior. One of the toughening strategies that have been proposed is to introduce a certain volume fraction of coarse grains (generally micron or sub-micron in size) into a nc matrix, leading to a microstructure with bimodal grain size distribution [58,59]. The coarse grain is softer than the nano-sized fine grains, and hence may help dissipate deformation strains and absorb energy during deformation, resulting improved ductility. From a micron scale perspective, a crack can be initiated and will propagate rapidly through the nanostructured grains during plastic deformation. The crack tip will be blunted when it reaches one of the ductile coarse grains. As the cracks propagate through the ductile phase, energy is absorbed and engineering ductility increases [58]. The existence of large grains may also help dissipate local stress concentration, thereby delaying the onset of fracture mechanisms. The nc Mg AZ80 synthesized via cryomilling and SPS processing contained a bimodal microstructure as shown in Fig. 7. Hence, for the purpose of analysis, the bimodal Mg AZ80 alloy could be considered as a composite, where the soft coarse grains are distributed in the hard nc matrix. To take into account the volume fraction and aspect ratio of the second phase in a composite, the Ramberg–Osgood equation can be used to describe the true strain, ε, during plastic deforming of a bimodal material [60]:

$$\varepsilon = \frac{\sigma}{E} + \alpha \varepsilon_0 \left(\frac{\sigma}{\sigma_N}\right)^n \tag{6}$$

where σ is the true stress, n is the stress exponent, E is Young's modulus of the bimodal alloy, α is a constant, ε_0 the strain of matrix, and σ_N is an asymptotic reference stress of a bimodal alloy, which depends on the volume fraction and morphology of the coarse grains. In view of the fact that Mg has a limited number of dislocation slip systems, the coarse grains are unlikely to contribute to ductility via increased dislocation activity. Instead, the coarse grains may help blunt a moving crack via energy dissipation. When a microcrack meets a coarse grain, propagation of the microcrack will be retard by blunting the crack or by delamination of interfaces between coarse-grained and fine-grained regions. Because the coarse grains grow from fine grains, the composition of the constituents is identical. There is no mismatch in thermal expansion coefficient or modulus between the fine and coarse grain regions in the bimodal cryomilled Mg alloys. Therefore, the interface energy between fine grains and coarse-grains is low, which will benefit energy dissipation.

4.3. Strengthening

Limiting the mobility of dislocations through the lattice provides a theoretical basis for the strengthening of metals. The onset of plastic deformation in Mg AZ80 alloys occurs when the applied stress reaches a critical value – their yield stress, σ_y. The increase in strength of cryomilled AZ80 alloys is mainly attributed to three factors: grain refinement, solid solution and dispersion strengthening. The crystallite size in Mg AZ80 alloys can be significantly reduced by cryomilling and retained after subsequent consolidation with SPS. On the basis of the dislocation pile-up mechanism of plastic deformation, the grain size dependence of the yield stress can be described by the Hall–Petch relationship [61,62]:

$$\sigma_{ys} = \sigma_0 + kd^{-1/2} \tag{7}$$

where d is the average grain diameter, σ_0 is a constant, and related to the CRSS for the easiest basal slip system operating for Mg alloys, and k is the stress intensity factor for plastic yielding, and associated with the CRSS for the more difficult non-basal slip systems [63], and as 0.279 MN/m$^{3/2}$ for Mg [30]. When the grain size is large

enough, the yield stress is approximately equal to the frictional stress, σ_0. The frictional stress for Mg–Al alloy may be approximated as 112 MPa via extrapolation [48]. The predicted increment in yield strength in the nc AZ80 by grain size refinement is 221 MPa when grain size is reduced to 69 nm, and 154 MPa when grain size goes up with a coarser grain to 495 nm. In order to aggregate the FG and CG contributions and thereby estimate the strength of this bimodal material, a simple linear combination of the rule-of-mixtures was used. In this case, $\sigma = \sigma_{fg}(1-f) + \sigma_{cg}f$, where f is the volume fraction of coarse grain (5%), σ_{fg} is the strength of the fine grain region, and σ_{cg} is the strength of the coarse grain region. The results of this weighted summation estimate the strength from the grain size contribution of the bimodal Mg AZ80 to be 218 MPa.

Solid solution strengthening occurs as a consequence of the interactions that take place between moving dislocations and the strain fields associated with misfit solute atoms. Solute atoms Al and Zn in Mg alloys change the lattice constants, a and c, and accordingly modify the binding forces. The dislocations may be pinned in the strain fields of solute atoms. Fleischer proposed that the yield strength increment for the magnitude of solid solution strengthening can be estimated through an equation that incorporates dislocation line energy and the average solute spacing [64]:

$$\Delta\sigma_s = \frac{G\varepsilon_s^{3/2}c^{1/2}}{700} \tag{8}$$

where c is the solute concentration in the alloy expressed as an atomic fraction, G is the shear modulus of solute, and ε_s is solid solution strengthening parameter combined the solute modulus and solute size effect on dislocations. For Mg AZ80 with 8 wt.% Al added in Mg, the predicted solid solution strengthening is about 3 MPa, which is significantly lower than the strengthening through grain refinement.

In addition, the strength of precipitate strengthened Mg alloys depends on the size, distribution and volume fraction of the precipitates. Al is the most significant elemental addition to Mg alloys, which can reduce the grain size and greatly enhance the mechanical properties of Mg alloys [2]. The nano $Mg_{17}Al_{12}$ intermetallic compound can precipitate, as shown in Fig. 9, and thereby the mechanical properties of Mg AZ80 can be further enhanced and play a considerable role. In general, as the Al content in Mg alloy increases, the formation of stable solid solutions and second phases increase, yield strength, ultimate strength, corrosion resistance and oxidation resistance all increase. Most importantly, Al promotes the formation of passive, complex Al oxide/hydroxide layers at the surface of Mg thereby reducing reactivity [1]. A small amount of Zn in Mg alloys does not generally lead to the formation of intermetallic compounds with either Mg or Al, but will reduce the solid solubility of Al in Mg and increase the amount of $Mg_{17}Al_{12}$ [24], which would strain lattice considerably. However, higher amounts of Al and Zn could reduce ductility due to the formation of brittle second phases.

The precipitated nano-sized $Mg_{17}Al_{12}$ particles will impede dislocation motion during deformation, resulting in strengthening. The precipitation strengthening can be estimated on the basis of the Orowan strengthening mechanism [65]:

$$\sigma_{Or} = M\frac{0.4Gb}{\pi(1-\nu)^{1/2}}\frac{\ln(\bar{d}/b)}{\bar{\lambda}} \tag{9}$$

where $M = 6.5$ [66] is the mean orientation factor, G is the shear modulus (16.6 GPa), b is the Burgers vector (0.321 nm), ν is the Poisson's ratio (0.28) [67], $\bar{d}$ is equal to $\sqrt{2/3}d$ and $\bar{\lambda}$ is the mean inter-particle distance given by $\bar{d}(\sqrt{\pi/4f}-1)$, where f is the concentration of the secondary phase dispersoids in the material (0.8%) [65]. Statistical analysis of the microstructures shows that the diameter of dispersoids in the coarse grain regions is 30–90 nm,

and hence we used average values 60 nm for the calculations. The average inter-particle distance is about 400 nm. Thus the strength contributions originating from nano-sized secondary phase dispersoids can be estimated to be 132 MPa.

Summing the contributions from grain size, solid solution and precipitation strengthening results in an overall estimated strength of 353 MPa. The numerical calculation described here incorporates some empirical constants for Mg alloy, which could lead to some discrepancies between real yield strength values (442.3 MPa) and those obtained from numerical predictions. When the grain size is further reduced to sub-nanometer scales (<20 nm), the strength values may deviate from the Hall–Petch relation [68]. The deviation may be attributed in part to the absence of dislocation pile-up and grain boundary deformation, such as grain-boundary sliding [69], which is sometimes reported to occur during plastic deformation of nc materials. The interactions among the various strengthening mechanisms described above are likely to be complex. The models employed here to aggregate the strength contributions into an overall strength are intended to provide insight within a reasonable range of certainty, that lead to the high strength exhibited in this nc Mg alloy. Nevertheless, the calculations do provide insight into the relative contributions of each mechanism.

5. Summary

In this present work, the effects of cryomilling on chemistry, particle size, and grain size of Mg AZ80 alloy powder have been studied. The microstructural evolution and mechanical response of the SPS consolidated samples processed at different sintering temperatures were investigated. The experimental results show that nc Mg powders with an average grain size of 40 nm can be prepared via cryomilling in 8 h. The chemical analysis results from cryomilled Mg powders showed an increase in the amount of N and Fe, while the oxygen content can be controlled within 0.065 wt.%. Deformation twinning was also observed in cryomilled AZ80 powder, and considered to contribute to the ductility of nc Mg AZ80 materials. The sustained mechanical deformation at cryogenic temperature increases energy storage in material, and thereby increases its strength.

The cryomilled Mg powder was consolidated using SPS at 250, 300 and 350 °C. A considerable increase in grain size at the particle interface and retained nc in internal particles was observed, resulting a bimodal microstructure. Inside of the coarse grains, nano-sized $Mg_{17}Al_{12}$ precipitates were observed. The measured maximum microhardness can reach to 146 HV, compressive yield strength reaches 442.3 MPa, and ultimate strength reaches to 546 MPa, which are significantly higher than those of conventional wrought Mg AZ80 alloys. The deformation behavior and the underlying mechanisms that govern nc Mg alloys were discussed in an effort to understand the fundamental phenomena in the nc Mg alloys prepared by cryomilling and SPS processing.

Acknowledgement

References

[1] H.E. Friedrich, B.L. Mordike, Magnesium Technology, Metallurgy, Design Data, Applications, Springer-Verlag, Berlin, Heidelberg, 2006.
[2] K.U. Kainer, Magnesium-Alloys and Technologies, Wiley–VCH Verlag GmbH & Co. KG aA, Weinheim, 2003.
[3] M.M. Avedesian, H. Baker (Eds.), Magnesium and Magnesium Alloys, ASM Specialty Handbook, ASM International, Materials Park, OH, 1999, pp. 3–6.
[4] R. Fink, in: K. Kainer (Ed.), Die-Casting Magnesium, Magnesium-Alloys and Technologies, Wiley–VCH Verlag GmbH & Co., Germany, 2003, pp. 23–44.

[5] S. Kamado, Y. Kojima, R. Ninomiya, K. Kubota, in: G.W. Lorimer (Ed.), Proceedings of the Third International Magnesium Conference, 1996, The Third International Magnesium Conference, 1996, Institute of Materials, Manchester, UK, 1997, pp. 327–342.
[6] A. Luo, M.O. Pekguleryuz, J. Mater. Sci. 29 (1994) 5259–5271.
[7] A. Akhtar, E. Teghtsoonian, Philos. Mag. 25 (1972) 897–916.
[8] H. Hoshikawa, S. Maki, S. Kamado, K. Yamada, Y. Kojima, 2nd Asian Symposium on Magnesium Alloys, Fukuoka International Congress Center, Fukuoka, Japan, 2007, pp. 136–137.
[9] H. Gleiter, Europhys. News 20 (1989) 130–133.
[10] E.J. Lavernia, B.Q. Han, J.M. Schoenung, Mater. Sci. Eng. A 493 (2008) 207–214.
[11] L. Lu, K. Raviprasad, M.O. Lai, Mater. Sci. Eng. A 368 (2004) 117–125.
[12] L. Lu, M.O. Lai, Y.H. Toh, L. Froyen, Mater. Sci. Eng. A 334 (2002) 163–172.
[13] B.Q. Han, T.G. Langdon, Mater. Sci. Eng. A 410–411 (2005) 435–438.
[14] R.B. Figueiredo, T.G. Langdon, Scr. Mater. 61 (2009) 84–87.
[15] W.J. Kim, S.I. Hong, Y.S. Kim, S.H. Min, H.T. Jeong, J.D. Lee, Acta Mater. 51 (2003) 3293–3307.
[16] J. Cízek, I. Procházka, B. Smola, I. Stulíková, R. Kuzel, Z. Matej, V. Cherkaska, R.K. Islamgaliev, O. Kulyasova, Mater. Sci. Eng. A 462 (2007) 121–126.
[17] B.Q. Han, J.Y. Huang, Y.T. Zhu, E.J. Lavernia, Acta Mater. 54 (2006) 3015–3024.
[18] V.L. Tellkamp, E.J. Lavernia, Nanostruct. Mater. 12 (1999) 249–252.
[19] J.A. Picas, A. Forn, L. Ajdelsztajn, J. Schoenung, Powder Technol. 148 (2004) 20–23.
[20] B. Huang, R.J. Perez, E.J. Lavernia, Mater. Sci. Eng. A 255 (1998) 124–132.
[21] O. Ertorer, T. Topping, Y. Li, W. Moss, E.J. Lavernia, Scr. Mater. 60 (2009) 586–589.
[22] F. Zhou, X.Z. Liao, Y.T. Zhu, S. Dallek, E.J. Lavernia, Acta Mater. 51 (2003) 2777–2791.
[23] M. Shahzad, L. Wagner, Mater. Sci. Eng. A 506 (2009) 141–147.
[24] A. Handbook, Magnesium and Magnesium Alloys, ASM International, Materials Park, OH, 1999.
[25] R. Orrù, R. Licheri, A.M. Locci, A. Cincotti, G. Cao, Mater. Sci. Eng. R: Rep. 63 (2009) 127–287.
[26] F. Sun, P. Rojas, A. Zúñiga, E.J. Lavernia, Mater. Sci. Eng. A 430 (2006) 90–97.
[27] D.B. Witkin, E.J. Lavernia, Prog. Mater. Sci. 51 (2006) 1–60.
[28] J.S. Benjamin, T.E. Volin, Metall. Mater. Trans. A 5 (1974) 1929–1934.
[29] B.J.M. Aikin, T.H. Courtney, Metall. Mater. Trans. A 24 (1993) 2465–2471.
[30] T.H. Courtney, Mechanical Behavior of Materials, 2nd ed., McGraw-Hill, New York, 2000.
[31] M.L. Lau, E.J. Lavernia, Mater. Sci. Eng. A A272 (1999) 222–229.
[32] C. Suryanarayana, Prog. Mater. Sci. 46 (2001) 1–184.
[33] H.P. Klug, L.E. Alexander, X-ray Diffraction Procedures, 2nd ed., John Wiley & Sons, New York, 1974.
[34] X.L. Wu, K.M. Youssef, C.C. Koch, S.N. Mathaudhu, L.J. Kecskes, Y.T. Zhu, Scr. Mater. 64 (2011) 213–216.
[35] D.H. Sastry, Y.V.R.K. Prasad, K.I. Vasu, Scr. Mater. 3 (1969) 923–928.
[36] Y. Wang, L.Q. Chen, Z.K. Liu, S.N. Mathaudhu, Scr. Mater. 62 (2010) 646–649.
[37] H.V. Swygenhoven, P.M. Derlet, A.G. Froseth, Nat. Mater. 3 (2004) 399–403.
[38] H. Somekawa, K. Hirai, H. Watanabe, Y. Takigawa, K. Higashi, Mater. Sci. Eng. A 407 (2005) 53–61.
[39] B. Li, E. Ma, Acta Mater. 57 (2009) 1734–1743.
[40] A.H. Feng, Z.Y. Ma, Acta Mater. 57 (2009) 4248–4260.
[41] X. Huang, K. Suzuki, N. Saito, Mater. Sci. Eng. A 508 (2009) 226–233.
[42] W.-J. Lai, Y.-Y. Li, Y.-F. Hsu, S. Trong, W.-H. Wang, J. Alloys Compd. 476 (2009) 118–124.
[43] F.P. Incropera, D.P. DeWitt, Fundamentals of Heat and Mass Transfer, John Wiley & Sons, Inc., New York, 1996.
[44] Z.A. Munir, U. Anselmi-Tamburini, M. Ohyanagi, J. Mater. Sci. 41 (2006) 763–777.
[45] F.R.N. Nabarro, Scr. Mater. 39 (1998) 1681–1683.
[46] A.J. Haslam, D. Moldovan, V. Yamakov, D. Wolf, S.R. Phillpot, H. Gleiter, Acta Mater. 51 (2003) 2097–2112.
[47] H.B. Huntington, in: A.S.N.A.J.J. Burton (Ed.), Diffusion in Solids, Academic Press, New York, 1975, p. 306.
[48] B.W. Chua, L. Lu, M.O. Lai, Philos. Mag. 86 (2006) 2919–2939.
[49] H.J. Fecht, Nanostruct. Mater. 6 (1995) 33–42.
[50] R.V. Mises, Z. Angew. Math. Mech. 8 (1928) 161–185.
[51] T. Obara, H. Yoshinaga, S. Morozumi, Acta Metall. Mater. 21 (1973) 845–853.
[52] G. Siebel, in: Beck (Ed.), Technology of Magnesium and its Alloys, Hughes, London, 1940.
[53] D.G. Westlake, in: R.E. Reed-Hill, J.P. Hirth, H.C. Rogers (Eds.), Deformation Twinning, Gordon & Breach, New York, 1963, p. 29.
[54] L. Lu, X. Chen, X. Huang, K. Lu, Science 323 (2009) 607–610.
[55] H. Somekawa, A. Singh, T. Mukai, Philos. Mag. Lett. 86 (2006) 195–204.
[56] J. Koike, R. Ohyama, T. Kobayashi, M. Suzuki, K. Maruyama, Mater. Trans. JIM 44 (2003) 445–451.
[57] G.J. Fan, H. Choo, P.K. Liaw, E.J. Lavernia, Acta Mater. 54 (2006) 1759–1766.
[58] V.L. Tellkamp, E.J. Lavernia, A. Melmed, Metal. Mater. Trans. A 32 (2001) 2335–2343.
[59] Y. Wang, M. Chen, F. Zhou, E. Ma, Nature 31 (2002) 912–915.
[60] W. Ramberg, W.R. Osgood, NACA Technical Report, TN 902, 1943, p. 1.
[61] E.O. Hall, Proc. Phys. Soc. (London) 64B (1951) 747–753.
[62] N.J. Petch, J. Iron Steel Inst. 174 (1953) 25–28.
[63] R.W. Armstrong, Acta Metall. Mater. 16 (1968) 347–355.
[64] T.H Courtney, Mechanical Behavior of Materials, McGraw-Hill, New York, NY, 2000.
[65] L.M. Brown, R.K. Ham, Strengthening Methods in Crystals, Elsevier, Amsterdam, 1971, p. 9.
[66] R. Armstrong, L. Codd, R.M. Douthwaite, N.J. Petch, Phil. Mag. 7 (1962) 45.
[67] B.Q. Han, D.C. Dunand, Mater. Sci. Eng. A 277 (2000) 297–304.
[68] M. Furukawa, Z. Horita, M. Nemoto, R.Z. Valiev, T.G. Langdon, Acta Mater. 44 (1996) 4619–4629.
[69] N.Q. Chinh, P. Szommer, Z. Horita, T.G. Langdon, Adv. Mater. 18 (2006) 34–39.